Conduction and switching mechanism in Nb_2O_5 thin films based resistive switches

2016 EPL 116 17003

(http://iopscience.iop.org/0295-5075/116/1/17003)

A LETTERS JOURNAL EXPLORING THE FRONTIERS OF PHYSICS

October 2016

EPL, **116** (2016) 17003
doi: 10.1209/0295-5075/116/17003

www.epljournal.org

Conduction and switching mechanism in Nb_2O_5 thin films based resistive switches

SWEETY DESWAL, ASHISH JAIN, HITESH BORKAR, ASHOK KUMAR[(a)] and AJEET KUMAR[(b)]

CSIR-National Physical Laboratory - Dr. K. S. Krishnan Marg, New Delhi 110012, India and Academy of Scientific and Innovative Research, CSIR-National Physical Laboratory Dr. K. S. Krishnan Marg, New Delhi 110012, India

received on 18 October 2016; accepted by J. F. Scott on 24 October 2016
published online 8 November 2016

PACS 73.40.Rw – Metal-insulator-metal structures
PACS 77.80.Fm – Switching phenomena

Abstract – We report unipolar resistive switching of $Pt/Nb_2O_5/Al$ device with orthorhombic crystalline phase prepared by reactive sputtering method. It showed non-volatile reproducible unipolar switching with ON/OFF resistance ratio of 10^3 or higher. The range of SET and RESET voltage was 1.0–2.0 V and 0.3–0.8 V, respectively, depending on devices and their dimension. The charge carriers followed Ohmic and space-charge–limited conduction (SCLC) behaviour in low-resistance state (LRS) and high-resistance state (HRS), respectively. An impedance spectroscopy analysis as well as a drift and diffusion of oxygen ion vacancy model are presented to explain the conducting filament formation and its rupture during the SET and RESET processes.

editor's choice

Introduction. – Two-terminal resistive switching (RS) devices are proposed to constitute the future non-volatile memory and logic devices [1–7]. The mechanism of the switching is based on formation and rupture of tiny conducting filament (CF) due to oxygen ion vacancies or defects movement in transition metal oxide (TMO) thin layers [4–7]. A complete understanding of the microphysics behind CF formation and rupture is required to have better control over the memory devices. The dynamics of CF formation and rupture has been explained on the basis of drift and diffusion process of oxygen ion vacancies (V_0) [8–10]. However, greater insight into the dynamics of CF is desired.

Transition metal oxides are the best suited material for the future RS memory devices due to their high-temperature stability, ease of film deposition, and compatibility with conventional semiconductor fabrication processes [11–13]. Crystalline phases of TMO's are proposed to have better device applicability with reduced switching variability due to improved structural uniformity [14]. Among all TMO's, Niobium pentoxide (Nb_2O_5) is a promising material for resistive switching devices in both amorphous [15–18] and crystalline phases [17,19] exhibiting unipolar [15,18], bipolar [16,19] and non-polar [20] resistive switching modes. The crystalline phase of Nb_2O_5 which may have reduced switching variability as compared to amorphous is very less explored. Also, very few reports [21] are available which studied conduction mechanisms of Nb_2O_5 thin film based resistive switching devices. Here we present, unipolar resistive switching behaviour of crystalline Nb_2O_5 thin film with *I-V* conduction analysis in both ON and OFF states. The detailed *I-V* characteristics and impedance spectroscopy analysis revealed Ohmic behaviour in low resistive state and SCLC type behaviour in high-resistance state. A drift *vs.* diffusion of oxygen ion vacancies based model is presented for CF formation and rupture during the SET and RESET switching steps. The impedance spectroscopic dielectric capacitance and loss analysis suggests the formation of conducting filament only in the low resistive state.

Experimental. – Niobium pentoxide (Nb_2O_5) thin films of thickness ~30 nm were grown on platinised Si wafer by reactive dc magnetron sputtering in 10% mass flow ratio of O_2 to Ar with deposition pressure of 1.9×10^{-2} mbar at room temperature. The Nb_2O_5 thin films were annealed at 750 °C for 3 h in O_2 flow of 2 sccm maintaining a pressure of $\sim1.0\times10^{-3}$ mbar. The ramp up and ramp down rate of the heater was 3.5 °C/min and 4.5 °C/min for the first 90 min, respectively, and afterwards around 3.8 °C/min (for cooling). The top electrode of Al (squares of $a\times a\ \mu m^2$ size; $a = 100$, 200, 300, 400 and

(a) E-mail: ashok553@nplindia.org
(b) E-mail: kumarajeet@nplindia.org

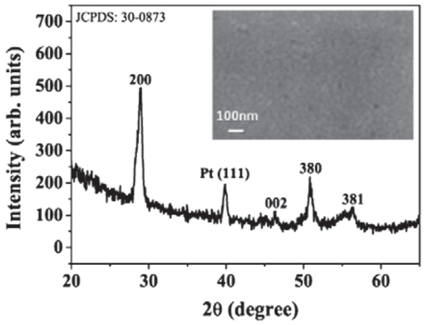

Fig. 1: XRD spectrum of the 30 nm Nb_2O_5 thin film annealed at 750 °C for 3 h deposited on platinised Si substrate. The inset shows the FE-SEM image of the same annealed Nb_2O_5 thin film. The morphology contains interlinked nano-domains, forming the crystalline phase.

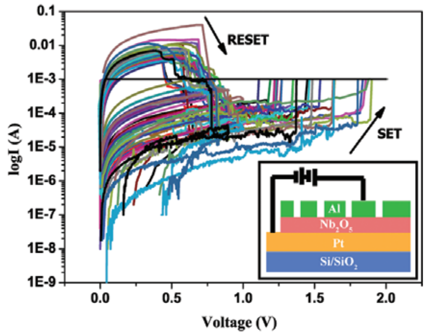

Fig. 2: (Colour online) The Semi-logrithmic I-V plot of the Pt/Nb_2O_5/Al device with $300 \times 300\,\mu m^2$ area. The plot shows reproducible, unipolar switching (25 cycles) for the same cell with SET (1.0–2.0 V) and RESET (0.3–0.8 V) traces. The inset shows the schematic of the device.

500 μm) was thermally evaporated over crystalline Nb_2O_5 thin films using shadow mask. The schematic of the fabricated Pt/Nb_2O_5/Al device is shown in inset of fig. 2.

The orthorhombic crystalline phase of Nb_2O_5 was confirmed by XRD patterns shown in fig. 1. The XRD peaks were indexed with JCPDS file 30-0873 for orthorhombic phase of Nb_2O_5, however, there were some differences in XRD peak positions compared to JCPDS file 30-0873, which may be due to lattice mismatch of Nb_2O_5 thin films with the substrate. The surface morphology of annealed Nb_2O_5 thin films was studied using FE-SEM technique as shown in the inset of fig. 1, that revealed the crystalline nature of Nb_2O_5 with interlinked nanostructures.

The room temperature electrical properties of Pt/Nb_2O_5/Al device were characterized with a two probe method using Agilent B2901A source meter. The voltage was applied to the top electrode (Al) while the bottom electrode (Pt) was grounded. The impedance spectroscopy was carried out using Hioki -50 impedance analyser 3532.

Results and discussion. – The current-voltage (I-V) characteristics of Pt/Nb_2O_5/Al device exhibit reproducible non-volatile unipolar resistive switching behaviour, shown in fig. 2. Initially, the Pt/Nb_2O_5/Al devices were in a high-resistance state, of the order of few MΩ. The electro-formation of the devices, the first SET, *i.e.*, switching from the initial high-resistance state to the low-resistance state occurred at around 6 V and the first RESET (*i.e.*, switching from LRS to HRS) was observed in the range 0.3–0.8 V. Thereafter, all subsequent SETs occurred in the range 1.0–2.0 V in positive voltage polarity. To avoid the permanent breakdown of the device, the current compliance limit (I_c) for the SET process was kept to be 1 mA. However, with the same current compliance, devices could not RESET either in positive or negative voltage polarity. For RESET, the I_c limit had to be increased ≥ 5 mA. All RESETs occurred in the voltage range 0.3–0.8 V in positive polarity with $I_c \geq 5$ mA. The probability of occurring SET and RESET was analysed and found to be in the voltage range 1.2–1.4 V and 0.5–0.6 V, respectively. The switching ON/OFF resistance ratio was 10^3 and higher. The non-volatile reproducible unipolar resistive switching obtained for 25 cycles on the same Pt/Nb_2O_5/Al memory cell is presented in fig. 2. The switching of the crystalline Nb_2O_5 is more reproducible and consistent as compared with amorphous Nb_2O_5 of nearly same thickness [20].

The log-log plot of unipolar I-V characteristic of Pt/Nb_2O_5/Al device is shown in fig. 3(a). The experimental data in LRS fitted linear with slope $\sim$1 suggesting Ohmic like conduction in LRS. The experimental data in HRS consists of three regions of linear fitting with different slopes, suggesting space-charge–limited conduction mechanism [22,23]. In HRS, more than ten current-*vs.*-voltage responses were analysed and curves were fitted to the relations that govern the space-charge–limited conduction mechanism.

In HRS, at low applied voltages ($V < V_{tr}$; the transition voltage from Ohm's law), J-V characteristics followed Ohm's law (linear fit with slope $\sim 1.3 \pm 0.14$). Also, the dielectric relaxation time ($\tau_{HRS} \sim 3.7$ ms), calculated using the relation $\tau = (\omega_{max})^{-1}$ from ImZ-*vs.*-frequency plot, of the charge carriers is in the range of milliseconds which is much larger than the dielectric relaxation time ($\tau_{LRS} \sim 85\,\mu$s) in LRS [22]. Hence, the carrier transient time, τ_{HRS} is several orders larger than τ_{LRS}. The injected carrier has no sufficient time due to large relaxation time to travel across the oxide thin film and also the injected carrier density is lower than the thermally generated carrier density, these conditions allow the charge carriers to obey Ohm's law and it follows eq. (1).

In the case of strong carrier injection, in the region of $V_{tr} < V$, the traps are partially filled up and space charge appears. The injected excess carriers dominate the thermally generated carriers since the injected carriers transit time is too short for their charge to be relaxed by the later carriers. In this condition, the SCL conduction is described by eq. (2) and it has a linear fit with slope of $\sim 2 \pm 0.28$.

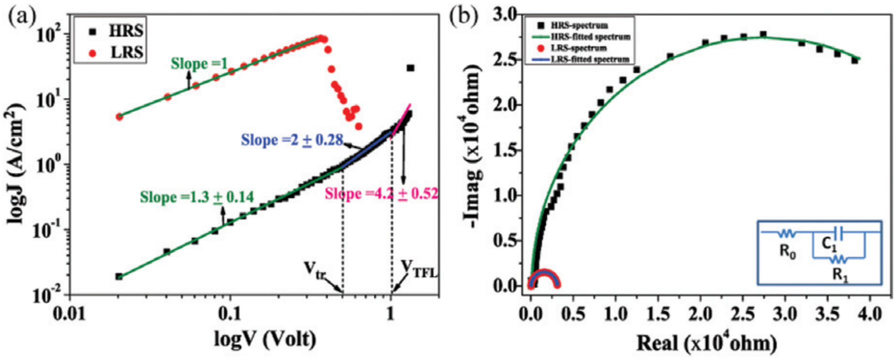

Fig. 3: (Colour online) (a) The log-log plot of *I-V* characteristics of the Pt/Nb_2O_5/Al device in LRS and HRS. Green line with slope $\sim$1 in LRS suggests Ohmic conduction. The HRS data with three regions of linear fitting (slopes of 1.3 ± 0.14, 2 ± 0.28 and 4.2 ± 0.52) indicates the SCLC mechanism. Here, V_{TFL} ($= 1\,\mathrm{V}$) is the trap filled limit voltage and V_{tr} ($= 0.5\,\mathrm{V}$) is the transition voltage from Ohm's law. (b) Nyquist plot in LRS (red dots) and in HRS (black squares). Green and blue lines are fitting in HRS and LRS, respectively. The lower inset shows the equivalent circuit used for the fittings.

In case of very strong injection, in the region of $V > V_{\mathrm{TFL}}$, all traps are filled and the conduction becomes the space charge limited (Child's law), where, injected carriers move freely in oxide thin film. The conduction relation is described by eq. (3) and it has a linear fit with slope $\sim 4.2 \pm 0.52$. These three regions in HRS are explained by three equations [22] given as follows:

$$J_{\mathrm{Ohm}} = q n_0 \mu \frac{V}{d}, \tag{1}$$

$$J_{\mathrm{TFL}} = \frac{9}{8} \mu \varepsilon \theta \frac{V^2}{d^3}, \tag{2}$$

$$J_{\mathrm{Child}} = \frac{9}{8} \mu \varepsilon \frac{V^2}{d^3}, \tag{3}$$

where q is the elementary charge, n_0 is the concentration of free charge carriers in thermal equilibrium, μ is electron mobility, V is the applied voltage, d is the thickness of thin film, ε is the static dielectric constant, θ is the ratio of the free carrier density to total carrier (free and trapped) density.

Impedance analysis. The impedance spectra were fitted in both LRS and HRS using EIS analyser software for further insight into switching mechanism. The impedance spectra were measured at room temperature in the frequency domain (1 kHz–1 MHz) at dc voltage bias of 0.1 V. The Nyquist plots (ImZ *vs.* ReZ) with fitting and fitted model for LRS and HRS are shown in fig. 3(b). An equivalent series circuit consisting of a resistance and parallel RC was used to numerically fit the impedance data, shown in lower inset of fig. 3(b). The fitting values of equivalent circuit elements in LRS are $R_0 = 40\Omega$, $R_1 = 3075\Omega$, and $C_1 = 1.95\,\mathrm{nF}$ and in HRS are $R_0 = 130\Omega$, $R_1 = 54933\Omega$, and $C_1 = 1.73\,\mathrm{nF}$.

The resistance, R_1 and capacitance, C_1 in parallel RC circuit corresponds to charge transport through bulk resistance and capacitance of oxide layer while the resistance R_0 represents the contact resistance of the micro probe station used for the measurements [24]. The capacitance

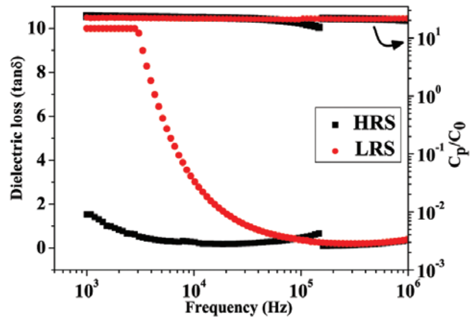

Fig. 4: (Colour online) The figure shows dielectric loss (left scale) and dielectric capacitance (right scale) of the device with frequency sweep in HRS (black squares) and LRS (red dots). The capacitance is almost constant in both HRS and LRS. However, one order higher magnitude of dielectric loss in LRS as compared to HRS is observed. The dielectric loss curve for LRS, in the low-frequency region, appears saturated due to limitation of the instrument.

C_1 and resistance R_0 remain almost unchanged while bulk resistance R_1 changes significantly (from $\sim 3\,\mathrm{k}\Omega$ to $\sim 55\,\mathrm{k}\Omega$) with switching from LRS to HRS. It is interesting to note that during the SET and RESET process only the bulk resistance of the system changed; however, the bulk capacitance remains almost same with several orders of change in dielectric loss (fig. 4). During the SET process, the parallel RC circuit suggests the formation of a current-filament which connects the top electrode to the bottom electrode. The completed filament, in LRS, divides the dielectric layer into small parallel capacitors which in turn add together to provide the same capacitance as in HRS. The same dielectric capacitance in both HRS and LRS with an order enhanced magnitude of dielectric loss in LRS suggests the formation of conducting filaments in LRS. It can be easily seen from fig. 4 that the bulk capacitance remains unchanged during switching cycles between HRS and LRS. The kink appeared in the HRS trace of fig. 4 may have occurred due to experimental fluctuation.

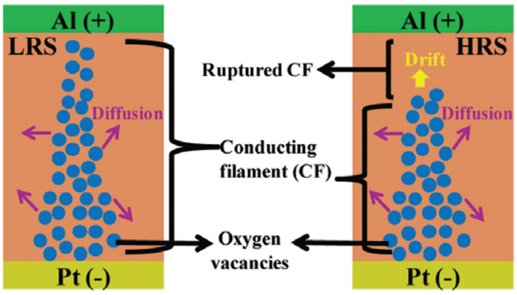

Fig. 5: (Colour online) The proposed model is presented to explain the non-linearity during the SET process. In HRS, the drift of oxygen vacancies dominates over diffusion due to the high electric field developed in the gap between filament and top electrode. After SET is reached, the Joule-heating–induced V_0 diffusion process dominates the V_0 drift.

Proposed model. The resistive switching involves oxygen ion vacancy redistribution in the RS layer and many groups have modelled such ion migration by drift-diffusion equations with thermally activated diffusivity and mobility [8,9]. Local e-field, temperature and oxygen ion vacancy concentration govern the drift and diffusion process of V_0. The conducting filament near the cathode (grounded electrode) has a greater interface area than that near the anode [25].

Therefore, the region near the anode interface experiences a higher current density and is getting ruptured, preferentially, because of more heating [26]. During the SET process, as shown in fig. 5, there exists a high electric field in the gap between the filament and the top electrode and it increases as the gap size decreases. Due to the high electric field, the V_0 transport is primarily governed by the drift process and the current profile of the device changes non-linearly. Once the LRS state is reached (fig. 5), the e-field is reduced and an Ohmic conduction pathway is created. This induces a linear change in the current profile of the device. In the LRS state, Joule heating (due to a higher reset current ≥ 5 mA) induces a lateral V_0 diffusion, away from the conducting filament [27], to rupture the filament. Moreover, oxygen ions diffusivity and generation of local heat near the anode junction of current-filaments and electrode lead to RESET of the system from LRS to HRS [8,9].

Conclusion. – In summary, the Pt/Nb_2O_5/Al device showed non-volatile, reproducible unipolar resistive switching in low-voltage ranges with ON/OFF resistance ratio of 10^3 or higher. The SET occurred in the range 1.0–2.0 V, while the RESET occurred in the range 0.3–0.8 V. The detailed analysis with fitting of *I-V* characteristics lead to Ohmic conduction in LRS and space-charge–limited conduction in HRS. The impedance measurement analysis of dielectric capacitance and dielectric loss suggests the formation of conducting filaments in LRS state. A drift and diffusion of oxygen ion vacancy model is presented to explain the non-linearity observed for CF formation during the SET process. The understanding of CF formation and rupture dynamics will help in the fabrication of more efficient resistive switching based memory devices.

* * *

We would like to thank Dr K. K. Maurya and Mr Himanshu Yadav for XRD measurements. We also acknowledge Ms Suniksha Gupta for her assistance in experiments. SD would like to acknowledge the financial support from the University Grant Commission (UGC) under senior research fellowship (SRF). This work was financially supported partly by DST INSPIRE Fellowship and partly by CSIR network project AQuaRIUS (PSC0110).

REFERENCES

[1] Yang J. J., Strukov D. B. and Stewart D. R., *Nat. Nanotechnol.*, **8** (2013) 13.
[2] Strukov D. B., Snider G. S., Stewart D. R. and Williams R. S., *Nature*, **453** (2008) 80.
[3] Sawa A., *Mater. Today*, **11**, issue No. 6 (2008) 28.
[4] Wedig A., Luebben M., Cho D.-Y., Moors M., Skaja K., Rana V., Hasegawa T., Adepalli K. K., Yildiz B. and Waser R., *Nat. Nanotechnol.*, **11** (2016) 67.
[5] Kim K. M., Jeong D. S. and Hwang C. S., *Nanotechnology*, **22** (2011) 254002.
[6] Waser R., Dittmann R., Staikov G. and Szot K., *Adv. Mater.*, **21** (2009) 2632.
[7] Yang J. J., Pickett M. D., Li X., Ohlberg D. A., Stewart D. R. and Williams R. S., *Nat. Nanotechnol.*, **3** (2008) 429.
[8] Larentis S., Nardi F., Balatti S., Gilmer D. C. and Ielmini D., *IEEE Trans. Electron Dev.*, **59** (2012) 2468.
[9] Kim S., Kim S.-J., Kim K. M., Lee S. R., Chang M., Cho E., Kim Y.-B., Kim C. J., Chung U.-I. and Yoo I.-K., *Sci. Rep.*, **3** (2013) 1680.
[10] Jeong Y., Kim S. and Lu W. D., *Appl. Phys. Lett.*, **107** (2015) 173105.
[11] Yoshida C., Tsunoda K., Noshiro H. and Sugiyama Y., *Appl. Phys. Lett.*, **91** (2007) 3510.
[12] Kim D., Seo S., Ahn S., Suh D.-S., Lee M., Park B.-H., Yoo I., Baek I., Kim H.-J. and Yim E., *Appl. Phys. Lett.*, **88** (2006) 202102.
[13] Yang J. J., Miao F., Pickett M. D., Ohlberg D. A., Stewart D. R., Lau C. N. and Williams R. S., *Nanotechnology*, **20** (2009) 215201.
[14] Hu C., McDaniel M. D., Posadas A., Demkov A. A., Ekerdt J. G. and Yu E. T., *Nano Lett.*, **14** (2014) 4360.
[15] Jung K., Kim Y., Park Y. S., Jung W., Choi J., Park B., Kim H., Kim W., Hong J. and Im H., *J. Appl. Phys.*, **109** (2011) 054511.
[16] Mähne H., Wylezich H., Hanzig F., Slesazeck S., Rafaja D. and Mikolajick T., *Semicond. Sci. Technol.*, **29** (2014) 104002.
[17] Mähne H., Berger L., Martin D., Klemm V., Slesazeck S., Jakschik S., Rafaja D. and Mikolajick T., *Solid-State Electron.*, **72** (2012) 73.

[18] Jung K., Kim Y., Jung W., Im H., Park B., Hong J., Lee J., Park J. and Lee J.-K., *Appl. Phys. Lett.*, **97** (2010) 233509.

[19] Chen L., Sun Q.-Q., Gu J.-J., Xu Y., Ding S.-J. and Zhang D. W., *Curr. Appl. Phys.*, **11** (2011) 849.

[20] Deswal S., Kumar A. and Kumar A., *AIP Conf. Proc.*, **1728** (2016) 020379.

[21] Kundozerova T. V., Grishin A. M., Stefanovich G. and Velichko A., *IEEE Trans. Electron Dev.*, **59** (2012) 1144.

[22] Chiu F.-C., *Adv. Mater. Sci. Eng.*, **2014** (2014) 578168.

[23] Lim E. W. and Ismail R., *Electronics*, **4** (2015) 586.

[24] Jiang X., Zhao Y., Chen Y., Li D., Luo Y., Zhao D., Sun Z., Sun J. and Zhao H., *Appl. Phys. Lett.*, **102** (2013) 253507.

[25] Kim K. M., Choi B. J. and Hwang C. S., *Appl. Phys. Lett.*, **90** (2007) 2906.

[26] Kim K. M., Choi B. J., Shin Y. C., Choi S. and Hwang C. S., *Appl. Phys. Lett.*, **91** (2007) 12907.

[27] Lee H. D., Magyari-Köpe B. and Nishi Y., *Phys. Rev. B*, **81** (2010) 193202.